C-band Observations of Supernova Remnants with SRT: I - Imaging performances

	Name	**Date**
Authors	E. Egron, A. Pellizzoni, M.N. Iacolina, S. Loru, S. Righini, A. Trois, R. Frau et al. on behalf of the Astronomical Validation Team and in collaboration with UNICA students: S. Boi & G. Murtas	15/04/15

DOCUMENT CHANGE RECORD					
Issue No.	**Issue date**	**No. of pages**	**Pages changed, added, deleted**	**Description of change**	**Contacts**
01	15/04/15	25	-	Issue 01	egron@oa-cagliari.inaf.it
					apellizz@oa-cagliari.inaf.it
					iacolina@oa-cagliari.inaf.it

Introduction

We report on observations of Supernova Remnants (SNR) with SRT in the frame of Astronomical Validation (AV) test activities. These tests are aimed to assess single-dish imaging performances of "SRT first light receivers" coupled with Total Power (TP) backend and related hw/sw subsystems/procedures (including innovative *ad hoc* imaging techniques based on OTF scans).

In this first note we focus on C-band imaging performances (image rms, dynamic range, RFI contamination, effective image resolution, morphologic comparison with literature data, etc.) resulting from the observation of SNR 3C157 (G189.1+3.0) and W44 (G34.7-0.4). A subsequent note will be specifically devoted to image calibration of the same targets and related issues *("C-band Observations of Supernova Remnants with SRT: II - Calibrations")*.

Image analysis is based on SRT Single Dish Imager (SDI), a state-of-the-art imaging data analysis software optimized for OTF scans, including automated baseline subtraction techniques and RFI rejection (Pellizzoni et al., in prep).

SNR are typically bright (10-100 Jy at 1 GHz) extended sources (0.5-1°) well suited for many AV tests. Integrated fluxes are typically available in literature up to 5-10 GHz, while SNR spatially resolved fluxes are largely unexplored above this frequency range, despite the growing challenging interest on high-energy GeV-TeV emission from SNR produced through Inverse Compton emission by radio-emitting electrons up to 50-100 GHz.

Located at about 1.5 kpc in the direction of the Galactic anticenter (Heiles 1984; Braun & Strom 1986), 3C157 (also named IC443) is one of the best-studied Galactic SNR. The large structure of the source extends over 0.75° and shows evidence of interactions with both atomic and molecular clouds (Snell et al. 2005). The discovery of a pulsar in X-rays with Chandra (Olbert et al. 2001) suggests a core-collapse origin of the SNR. The radio flux density at 1 GHz is about 160 Jy (for an exhaustive reference list see Green (2014), *http://www.mrao.cam.ac.uk/surveys/snrs/snrs.G189.1+3.0.html*).

W44 is a bright radio SNR ($S_{1GHz} \sim 230$ Jy) located in the Galatic plane at about 3.0 kpc. Formed nearly 10^4 yrs ago (Jones et al. 1993), it presents an asymmetric morphology of about 0.5° in size. It belongs to the "mixed morphology" class of remnant, characterized by a highly filamentary radio shell (synchrotron emission) and a central thermal X-ray emission (Smith et al. 1985). W44 harbours a young radio pulsar PSR B1853+01 (Wolszcan et al. 1991) compatible with the estimated age of the SNR and a pulsar wind nebula. It also represents a rare case since it physically interacts with its parent molecular cloud complex (Seta et al. 1998).

Due to the availability of a relatively wide amount of multi-wavelength data, their complex and challenging morphology, and their complementary visibility at the SRT site (transit at LST=19h for W44 and LST=06h for 3C157; we used CASTIA for SRT sources visibility; Vacca et al. 2013), SNR W44 and 3C157 represent ideal targets for the verification and exploitation of SRT single-dish imaging potentialities for the study of extended Galactic sources.

In §1 we provide a detailed overview of C-band SRT observations of W44 and 3C157 including OTF schedule parameters performed through Nuraghe antenna control software (Righini et al. 2015). An introductory overview of the main features of the data analysis software SDI and data reduction procedure is provided in §2, while results are presented in §3 together with images comparison with literature data. Open issues/problems evinced from the reported tests are summarized in §4. Links to repository

of relevant data products discussed in this note and SRT images of W44 and 3C157 are reported in appendix.

1 – SRT Observations

We carried out mapping of SNR 3C157 and W44 through On-the-Fly scans (OTF). This technique implies that the data acquisition is performed with continuity (sampling time of a few tens ms) at constant speed (typically a few degrees/min), repeatedly scanning the sky in both right ascension (RA) and declination (DEC) directions (each passage is called "subscan"). The above parameters typically imply the acquisition of >10-20 samples/beam for each subscan passage (largely oversampling the beam w.r.t. Nyquist sampling) allowing accurate evaluation of flux errors. In addition to ease a careful errors evaluation, beam oversampling allow us to efficiently reject outliers measurements ascribed to RFI.

The length of the subscans is chosen accordingly to the size of the source (typically of the order of 0.5-1° for SNRs). In order to properly reconstruct the morphology of the observed source and its associated flux, the subscan-dependent baseline (background flux) must be correctly subtracted. Ideally, each subscan should be free from significant source contribution (and RFI contamination) for 40-60% of its length/duration, in order to properly identify and subtract the baseline component. This requirement is not trivially granted for targets located in crowded regions of the Galactic Plane, as for the case of W44.

The observations of 3C157 and W44 were performed in C-band, at 6.9 GHz (LO set at 6800 MHz), with the Total Power backend. The active surface was set in the shaped configuration to offer a better illumination of the Gregorian focus and to adjust the panels of the primary mirror in function of the elevation. The minor servo system was configured in tracking mode to correct the sub-reflector position according to its pointing model. We selected a bandwidth of 730 MHz (680 MHz effective) and a sampling/integration time of 40 ms. For 3C157, the subscan length was set to 1.5° (= 90') in both RA and DEC, accounting for the size of 3C157 of about 45' and baseline subtraction requirements. W44 is a slightly less extended source (about 30'), and the subscan length was set to 1.2° in RA and 1° in DEC, accounting also for nearby sources contamination on the Galactic Plane. Each subscan duration was scheduled to 22.5 sec for the first source, and 18 sec (RA) and 15 sec (DEC) for the second one, which implies a OTF speed of 4'/sec. Two consecutive subscans were separated by an offset of 0.01°, which implies that 4.5 passages were carried out per beam on average, and about 17 samples per beam per scan (assuming a beam size of 2.7' in C-band) were taken. The duration of additional dead time/slew time varied between the observations, lasting for about 10-16 sec at the end of each subscan (typically up to 30-40% of overall duration). The total duration of an observation (single map RA+DEC) was about 3 hours for 3C157, and about 2 hours for W44. A clear weather is necessary to produce maps of quality in C-band. More details about the observations are reported in Tables 1 and 2.

3C157		Filename (UTC)	Elevation (deg)	Azimuth (deg)	Map size Fov (deg)	Total duration (min)	Effective duration (min)	Dead time (s)
27/05/14	RA	143916	66.3 - 54.8	230.5 - 252.6	1.50*1.28	68.5	46.8	10.2
	RA	162637	46.7 - 31.5	259.8 - 275.9	1.50*1.61	85.8	55.2	12.2
03/06/14	RA	091116	40.0 - 55.7	91.3 - 110.7	1.50*1.50	80.8	55.2	10.2
	DEC	103246	54.7 - 69.8	107.2 - 141.5	1.50*1.50	80.8	55.2	10.2
17/10/14	RA	011400	51.1 - 67.4	101.8 – 136.7	1.50*1.50	95.9	55.2	16.2
	DEC	034029	71.8 - 66.5	162.8 – 232.6	1.50*1.50	95.9	55.2	16.2
	RA	053024	64.1 - 47.1	235.9 – 260.9	1.50*1.50	95.8	55.2	16.2
10/12/14	RA	193500	27.4 - 43.4	81.4 - 96.7	1.50*1.50	80.9	55.2	10.2
	DEC	205629	42.4 - 59.5	94.0 - 115.2	1.50*1.50	80.9	55.1	10.3

Table 1 : Summary of the observations (good weather) of SNR 3C157 with SRT in C-band.

W44		Filename (UTC)	Elevation (deg)	Azimuth (deg)	Map size Fov (deg)	Total duration (min)	Effective duration (min)	Dead time (s)
09/07/14	RA	231416	52.3 - 49.8	181.4 - 201.3	1.20*1.00	46.4	29.4	10.1
	DEC	000118	49.7 - 45.5	199.9 - 219.0	1.20*1.00	49.5	29.1	10.1
16/09/14	RA	161318	39.8 - 46.8	129.0 - 147.9	1.20*1.00	56.6	29.4	16.1
	DEC	171034	46.4 - 52.0	146.0 - 171.0	1.20*1.00	61.7	29.2	16.1
11/09/14	RA	154928	32.8 - 41.4	118.8 - 134.4	1.20*0.99	55.9	29.2	16.0
	DEC	164605	40.9 - 49.4	132.6 - 154.2	1.20*1.00	61.6	29.1	16.0
	RA	175701	49.8 - 51.4	155.4 - 179.5	1.33*1.00	56.5	29.4	16.1
	DEC	185411	51.4 - 49.9	177.9 - 204.1	1.20*1.06	61.5	29.2	16.1
	RA	201140	48.5 - 41.5	208.3 - 226.8	1.20*1.00	56.5	29.3	16.1
	DEC	210849	41.4 - 31.8	225.8 - 242.6	1.20*1.06	61.6	29.3	16.1

Table 2 : Summary of the observations (good weather) of SNR W44 with SRT in C-band.

2 - Data reduction and analysis

Data analysis was performed through the SRT Single Dish Imager (SDI; user manual, Pellizzoni et al. *in prep*), a tool designed to perform continuum (and in perspective spectro-polarimetric) imaging, optimized for OTF scan mapping, and suitable for all SRT receivers/backends. SDI provides an automatic pipeline (quicklook analysis) and interactive tools for data inspection, baseline removal, RFI rejection and image calibration (standard analysis). Written in IDL (porting in Python is undergoing), it generates SAOImage DS9 (*http://ds9.si.edu*) output FITS images suitable for further analysis by standard astronomy tools. The core of the SDI features/performances is to fully exploit the availability of a significant number of measurements per beam (and then per pixel, typically chosen as about 1/3 of the beam FWHM), in order to have a straightforward evaluation of statistical errors (through standard deviation of the measurements in each pixel).

The analysis procedure with SDI typically involves the following general steps:

1) Running SDI quicklook procedure using simplified automated baseline subtraction algorithms ("adjusted" linear fit, see below) and rough RFI rejection (RFI=outliers

above 5 sigma threshold w.r.t. average measurements within about 1/4 beam solid angle). This procedure is also typically run on-line during the observations.

2) Interactive inspection and analysis scan-by-scan in order to identify and adjust anomalies in baseline subtraction and RFI rejection (e.g. discarding corrupted subscans, further manual flagging/unflagging of RFI).

3) Refined automated analysis with (time consuming) advanced baseline subtraction algorithms (see below).

4) DS9 FITS image production and analysis through SAOImage (rms, dynamic range, brightness profiles etc.).

5) Dedicated IDL tools/procedure to accurately evaluate measurements errors for each map pixel and their propagation for the estimation of derived quantities (e.g. integrated fluxes etc.), including systematic effects.

The "Adjusted linear fit" of the baseline adopted in the quick-look procedure is empirically based on the computation of the angular coefficient of the baseline slope taking only 80% of the samples with the lowest counts (thus approximately discarding major RFI events and strong source contamination), and then normalizing the linear fit to the average of the 15% lowest counts samples. This rough-and-dirty baseline subtraction method provides reasonable image accuracy in very short computation time (can be even run on-line during scan acquisition, updating the image during nearly real-time scan-by-scan acquisition), for most mapping observations/schedules. It provides basic/starting baseline estimate for further manual and more accurate automated analysis.

"Advanced" baseline subtraction algorithms are adopted for the final refinement of the analysis. A baseline "fitness" parameter (BF) is defined as the number/percentage of scan samples being within a RMS (i.e. 1 sigma level of the baseline fluctuation) of a given baseline linear fit. Higher the BF value, better the accuracy of the baseline model. BF parameter is maximized through a trials loop on the angular coefficient and normalization of the linear fit. For example, linear fit trials performed on a subscan on the empty sky, converge to a maximum BF=68% (i.e. 68% of the samples are within 1 sigma/RMS from the best linear fit), as theoretically expected.

In principle, if at least 50% of the scan samples are related to the baseline (i.e. if <50% of the samples are significantly contaminated by RFI and astrophysical sources), this procedure provides mathematically exact results though BF maximization: manual inspection/trimming of the baseline cannot provide more accurate (and rigorous) results.

The requirement of 50% "source/RFI-free" for the scan samples cannot be trivially fulfilled on subscan performed along crowded regions as -e.g.- the Galactic Plane. In this case, SDI tries to solve anyway for baseline model disentangling among possible incorrect solutions (e.g. an extended source "plateau" filling most of the subscan, miming the baseline level and maximizing BF in underhanded wrong manner).

Concerning RFI rejection, SDI provides an automatic and interactive RFI flagging procedure. The automatic procedure consists in splitting the map in sub-regions, which correspond to adjacent solid angles in the sky. These areas have to be inferior to the beam size (typically 1/4-1/5 of BWHM) in order to avoid discarding actual fluctuations from the source, but large enough so that they include a significant (typically >10) number of measurements. An algorithm calculates the average sample values inside each region,

considering 90% of the lowest counts samples (in order to have average values unbiased from strong RFI). The "outliers" samples presenting a count level above a standard deviation-based threshold (typically 3-5 sigma level above average) are then flagged as RFI. The user chooses the sub-region size and the standard deviation level for the automatic procedure. More details on SDI algorithms and procedures are reported in the SDI user manual (Pellizzoni et al., *in prep.*).

In the following, we present the results of the automated data reduction of 3C157 and W44 using SDI.

A quicklook of the maps was performed on-line during the observations in order to assess the quality of the data. Bad observations related to inadequate weather conditions were discarded. For instance, an observation of 3C157 was performed on 2014 April 3 when the sky was cloudy. The presence of clouds clearly affects the quality of the map, as testified by Figure 1, which constrains us to exclude this data set for the rest of the analysis. Our weather requirement in order to shortlist good data was a clear sky (or at least an uniform coverage).
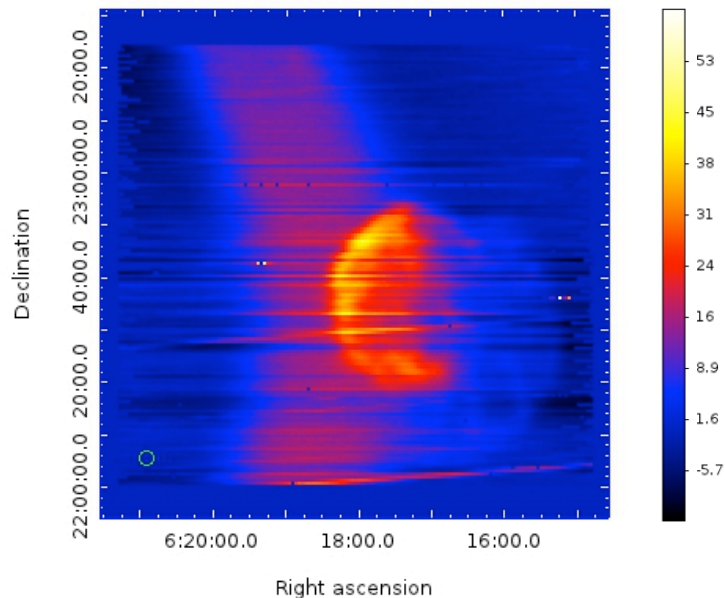

Figure 1: Quicklook of 3C157 (only RA) obtained during the observation performed on 2014 April 14, using the adjusted linear fit of the baseline. Clouds appear as a purple bow on the map and strongly affect the data.

We then applied the advanced baseline-subtraction method on the good quality observations of 3C157 and W44 reported in Tables 1 and 2. The RFI rejection was performed using sub-regions of 1' and a standard deviation level of 5 sigma. The map resolution was chosen at 0.6' (pixel size). Figures 2 and 3 show the individual maps (RA+DEC) of 3C157 and W44, respectively, obtained during the different observational sessions.
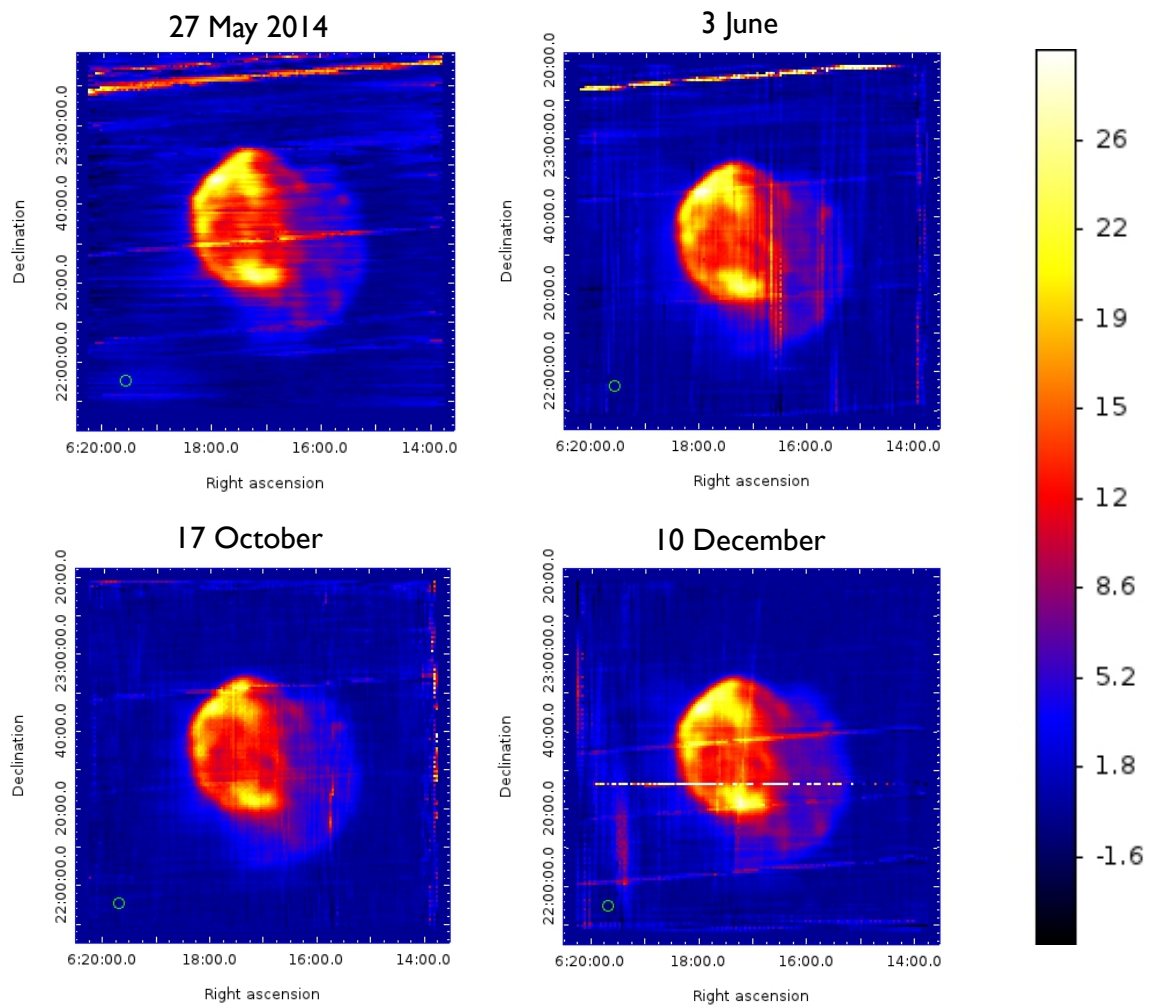
Figure 2 : Individual maps of 3C157 corresponding to Table 1, obtained using the advanced baseline-subtraction method. The bright lines visible on each map correspond to RFI still present, even if most of them were removed by merging RA and DEC data.
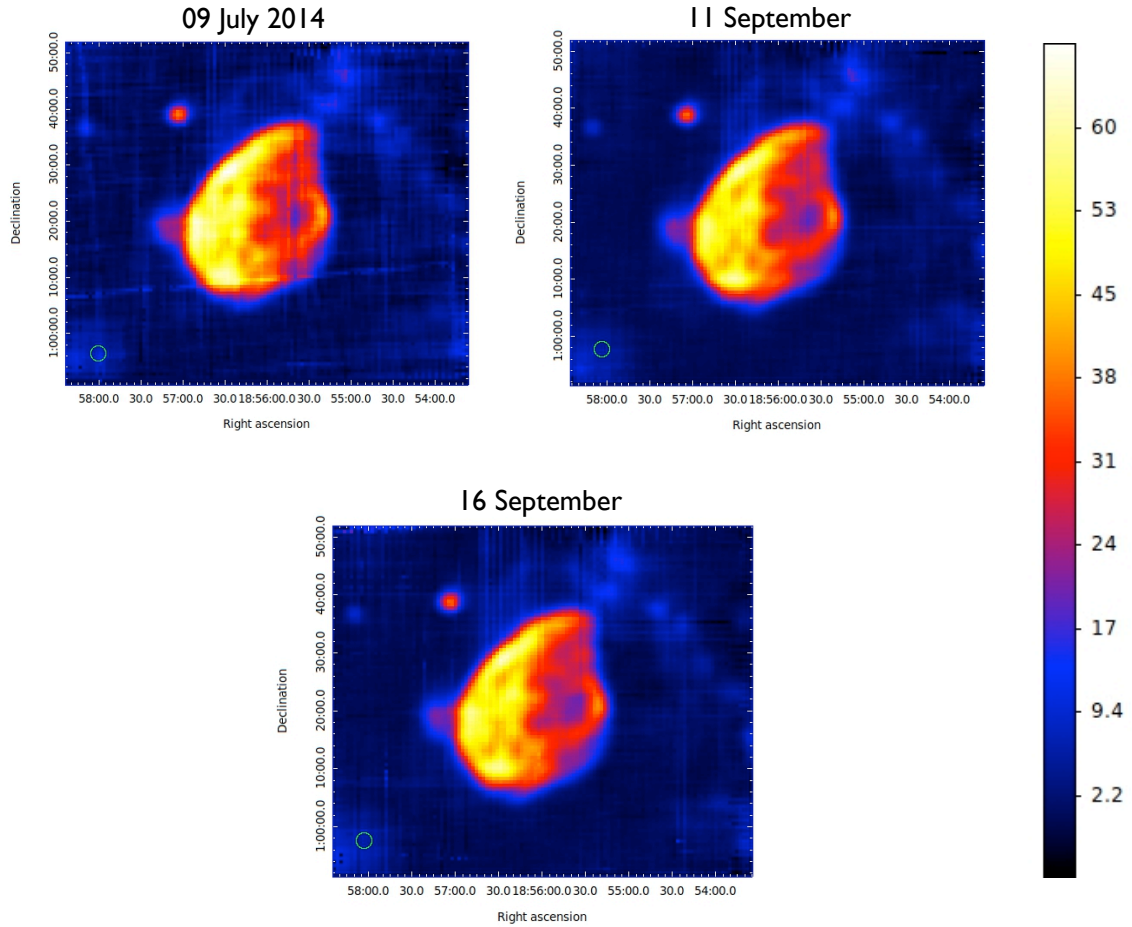
Figure 3 : Individual maps of W44 obtained using the advanced baseline subtraction. See Table 2 for the details about the observations.

We estimated the 1 σ rms noise, which corresponds to the count values in the dark blue areas of the maps (average zero counts on empty sky), and the dynamic range (assumed as maximum count value divided by the rms) for each map. We considered rectangular areas where the count values were the lowest to determine the rms. The values are reported in Table 3.

3C157	Rms	Dynamic range
27/05/2014	0.47	62.1
03/06/2014	0.46	66.5
17/10/2014	0.33	78.0
10/12/2014	0.24	116.7

W44	Rms	Dynamic range
09/07/2014	0.71	87.3
11/09/2014	0.30	200
16/09/2014	0.38	155.3

Table 3: Rms and dynamic range for the individual maps of 3C157 and W44 presented in Fig. 2 and 3, respectively.

The production of a map of an extended source typically requires observations that last for a few hours. As a result, the elevation and so the baseline slope significantly changes. In Figure 4, we plot the slope of the baseline in function of the elevation for each data set of both sources.
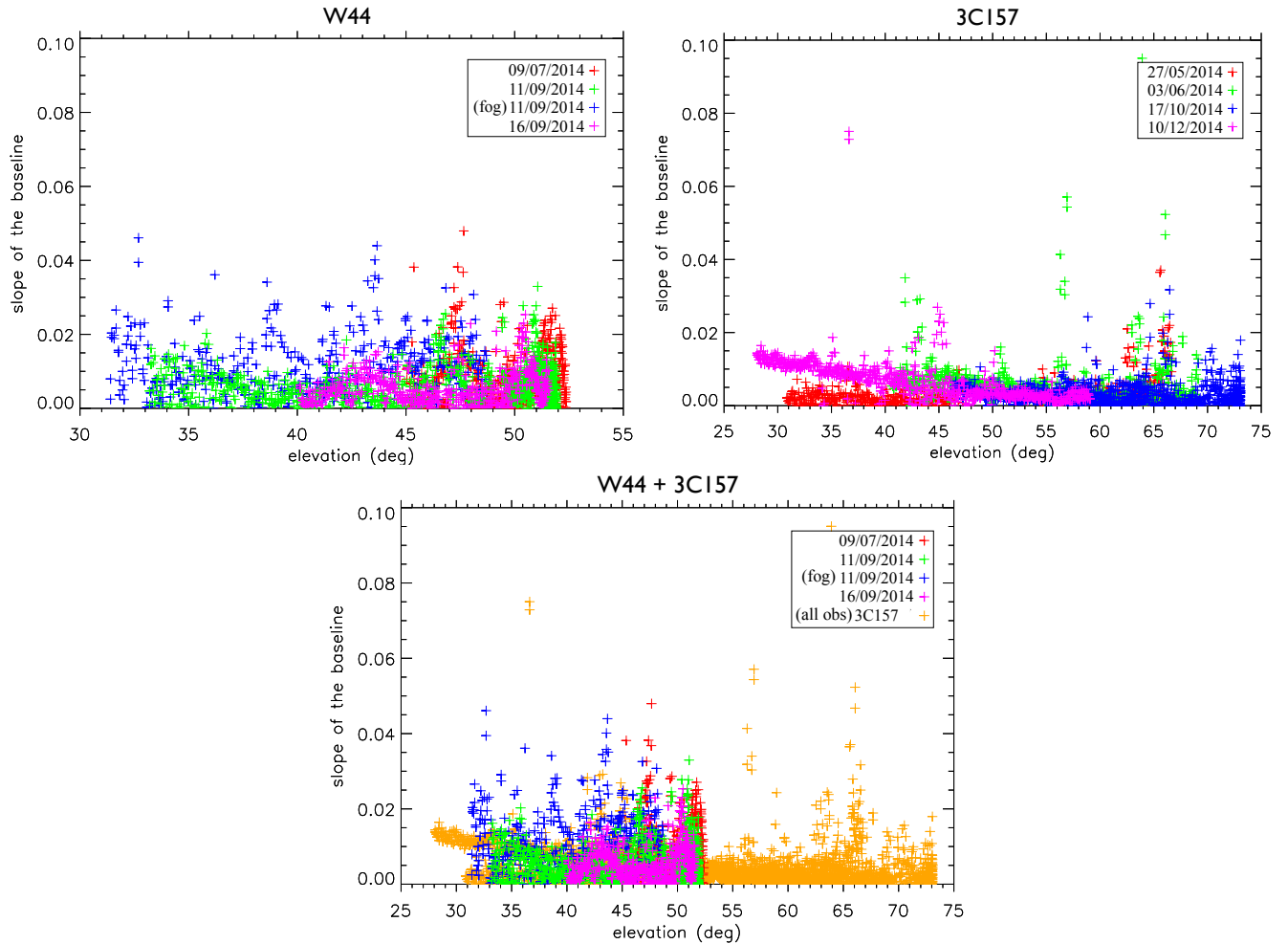
Figure 4: Slope of the baseline in function of the elevation for the different observations of W44 (upper left) and 3C157 (upper right). The third plot corresponds to the data of W44 (4 data sets with a color for each observation) plus 3C157 (all observations are in yellow).

In the case of W44, the distribution of the data corresponding to the last observations performed on 11/09/2014 (when the fog appeared) is different from the other data sets. The opacity seems to be responsible from this notable difference. As far as 3C157 is concerned, the data of each observation are distributed following lines with a different slope. For both sources, outlying points form peaks, independently from the data sets, at some elevations such as 35°, 43° and 47°. Two other prominent peaks are visible in the 3C157 data at about 57° and 65°. This possible anomalies required manual inspection of the baselines related to these subscans: no apparent problems with data and/or baseline subtraction were reported although further analysis are ongoing to shed light on these anomalous baseline slopes.

3 – Results

This section is dedicated to the inspection of the total/integrated maps of 3C157 and W44 obtained with SRT using SDI. We then compare the maps with the literature to better

understand the complex morphology of these SNRs and to assess imaging performances of SRT.

A) SNR 3C157

The quality of a map is highly improved by adding the data performed during the different observational sessions, in particular for what concerns the RFI rejection and the S/N. Only RFI located on the edge of the map are removed with more difficulty. The map of 3C157 resulting from the simultaneous data analysis of the four data sets previously mentioned is shown in Figure 5. In total, about 40.5 passages per beam were performed. The corresponding rms noise and dynamic range are 0.22 counts and 125.5, respectively, that we can compare with the values reported on Table 3 for each individual map.
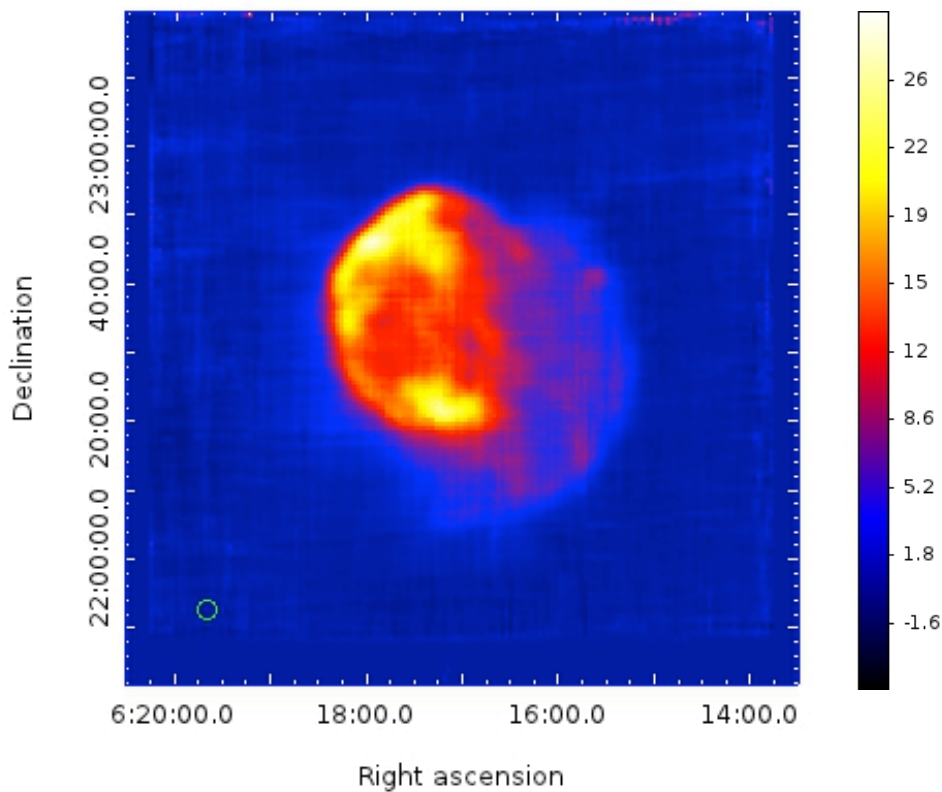
Figure 5: Global map of 3C157 using the advanced baseline subtraction method on the 4 data sets summarized in Table 1. The 1.5°*1.5° map is composed of 882*454 subscans (RA/DEC).

In order to highlight the role of the automatic RFI rejection method in SDI, we present in Figure 6 the map of 3C157 obtained without this procedure. The presence of strong RFI obviously deteriorates the quality of the map, which demonstrates the efficacy of the automatic RFI rejection method in SDI. About 6.6% of the samples were ascribed to RFI and flagged.
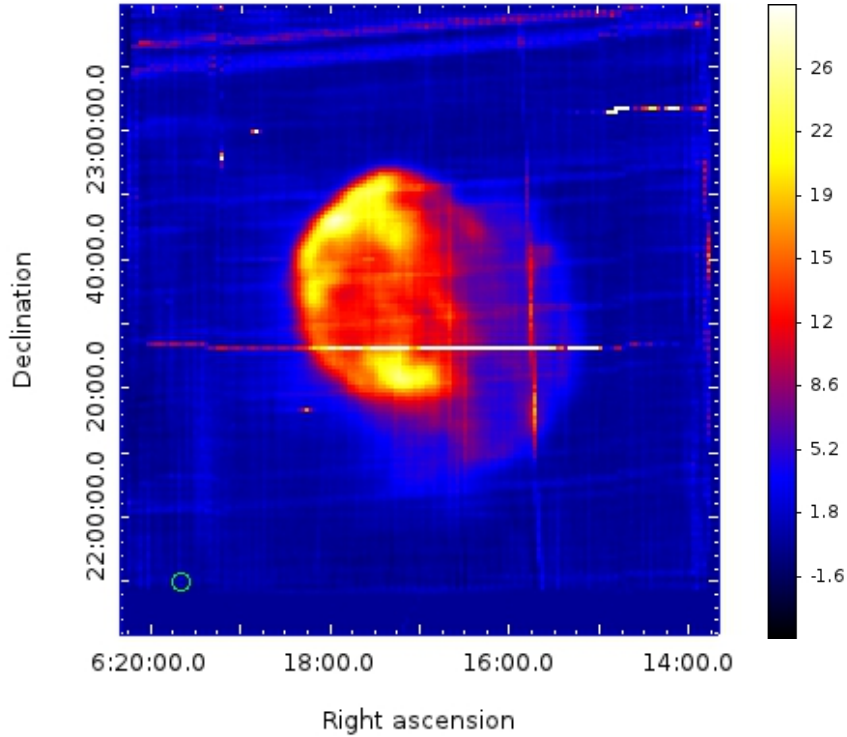
Figure 6: Global map of 3C157 obtained without using the method of RFI rejection.

We produced a histogram of the count values to infer the areas where the flux is uniform, as illustrated in Figure 7. This gives a precise estimate of the average rms noise level (region *a)* in Fig.7), which is related to the full width at half maximum of the main peak (see Figure 8): *rms=FWHM*/2.3. It is reckoned at about 0.17 counts (dynamic range=162), to be compared with the rough estimate obtained with DS9 at (0.22 counts).

Two other prominent peaks at about 2-3 counts and 6-8 counts are visible on the histogram. We identified these regions on the map; the first one is associated to the light blue pixels forming the faint halo on the edge of the supernova remnant (region *b*), whereas the second one corresponds to the purple filaments (region *c*). A third peak at about 11 counts indicates the red pixels on the map (region *d*).
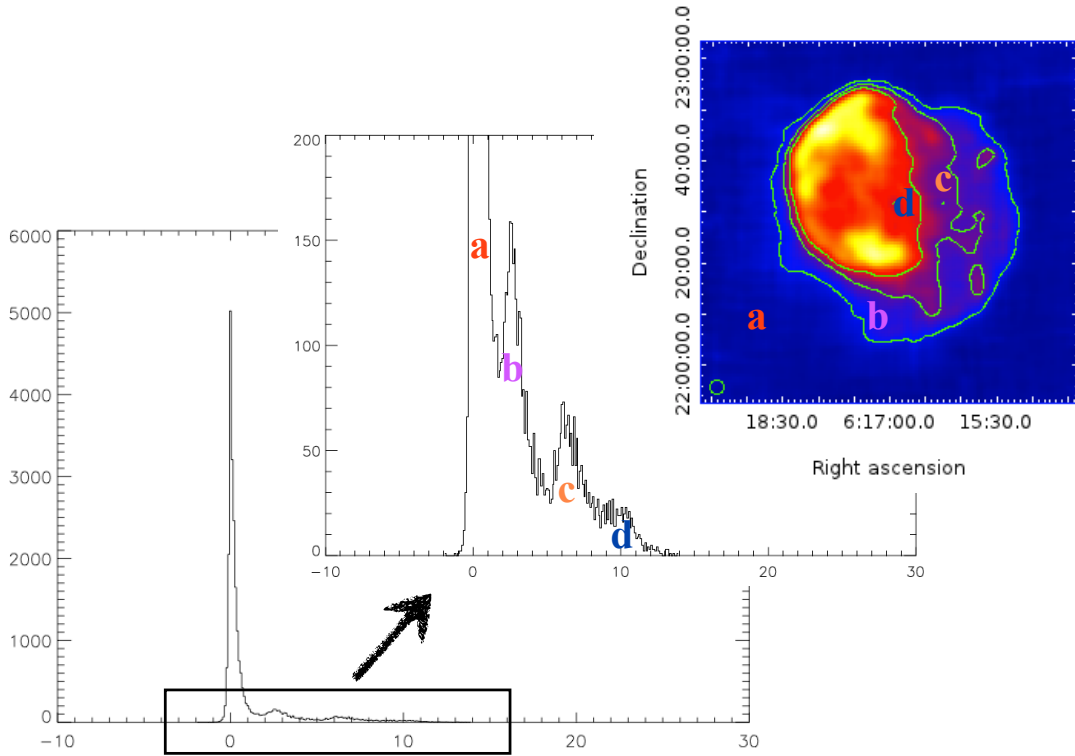
Figure 7: Count histogram obtained with a binning of 0.1. The different peaks (a,b,c,d) indicate regions on the map were the flux is uniform. The corresponding contours are identified on the map of 3C157.
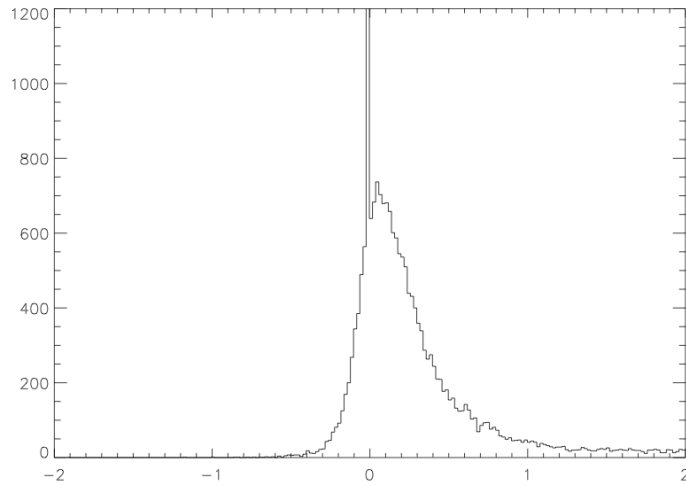

Figure 8: Zoom of the main peak of the count histogram, with a binning of 0.02. The full width at half maximum of the peak gives an estimate of the average rms (the narrow peak at 0 counts is unphysical and related to the edge of the rectangular map not fully covered by the observations).

We compared the map of 3C157 obtained with SRT with those resulting from the radio continuum observations conducted by Effelsberg, Urumqi, the National Radio Astronomy Observatory Very Large Array (VLA) and Arecibo. The details of the observations are reported in Table 4.

	Effelsberg	**Urumqi**	**VLA**	**VLA**	**Arecibo**	**SRT**
Date obs	1999-2000	2004-2009	03/1996 07/1996	02/12/2001	31/10/2001 03/11/2001	27/05/2014 03/06/2014 17/10/2014 10/12/2014
Duration			40 min 30min	6.3h (54min per pointing)		Total 12.8h
Frequency	868 MHz	4.8 GHz	330 MHz	1.4 GHz	1.4 GHz	6.9 GHz
Bandwidth	30 MHz	600 MHz		1.6 MHz	3.1 MHz	730 MHz
HPBW	14.5'	9.5'		40''	3.9'	2.7'
Type of obs		Raster map	Configurations C and D	Configuration D	OTF – TP	OTF - TP

Table 4: Summary of the observations of 3C157 conducted by Effelsberg, Urumqi, the VLA, Arecibo and SRT. Note: VLA's configurations C and D correspond to the antenna separation of 3.4km and 1km, respectively.

Single-dish observations of SNR 3C157 were made by the Effelsberg 100m telescope at 35cm wavelength (Reich et al. 2003), and by the Urumqi 25m telescope during a 6cm polarization survey of the Galactic plane (Gao et al. 2011). The resulting images are compared with the map obtained with SRT at 6.9 GHz in Figure 9. The three observations highlight the presence of different strong intensity regions in the SNR. The interaction of 3C157 and the HII region (S249) located at the north of the remnant are clearly visible on the maps obtained with Effelsberg and Urumqi, whereas SRT offers more details on the morphology of the supernova remnant at the observed frequency thanks to the lower angular resolution (see the half power beam width (HPBW) values reported in Table 4).

SNR 3C157

a) Urumqi at 4.8 GHz
b) Effelsberg at 868 MHz
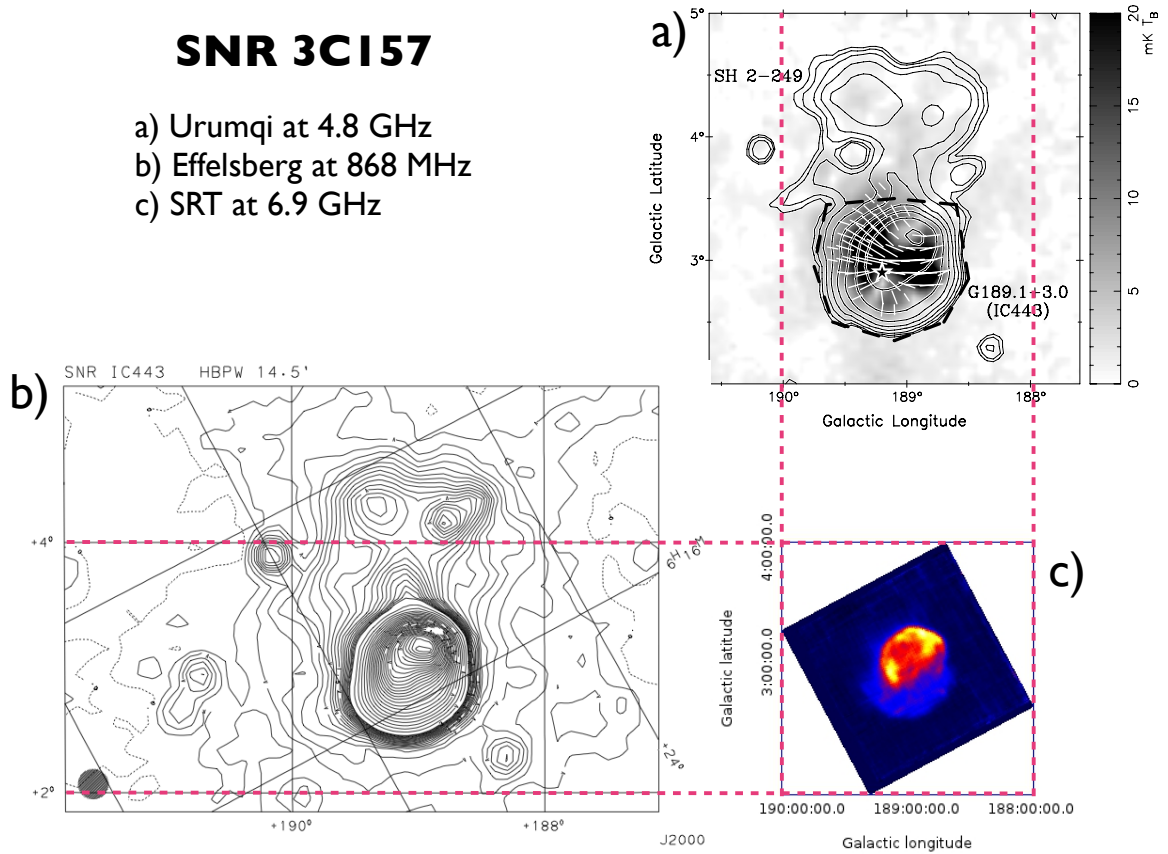c) SRT at 6.9 GHz

Figure 9: a) Radio continuum and polarization image of 3C157 obtained with the Urumqi 6cm polarization survey (Gao et al. 2011). The polarization intensity is indicated with the grey scale and is overlaid by the intensity contours. The star indicates the pulsar and pulsar wind nebula. b) Contour plot of 3C157 observed at 868 MHz with Effelsberg (Reich et al. 2003). c) SRT observation at 6.9 GHz in galactic coordinates. Red dot lines indicate the same coordinates.

VLA and Arecibo data were combined together to achieve an extremely good sensitivity and angular resolution of about 40". In order to cover the full remnant, seven separated pointings were performed with the VLA, then combined together to produce a mosaic. These observations provided details of the complex morphology of 3C157 at low frequencies, revealing features previously unknown (Lee et al. 2008), as shown in Figure 10.
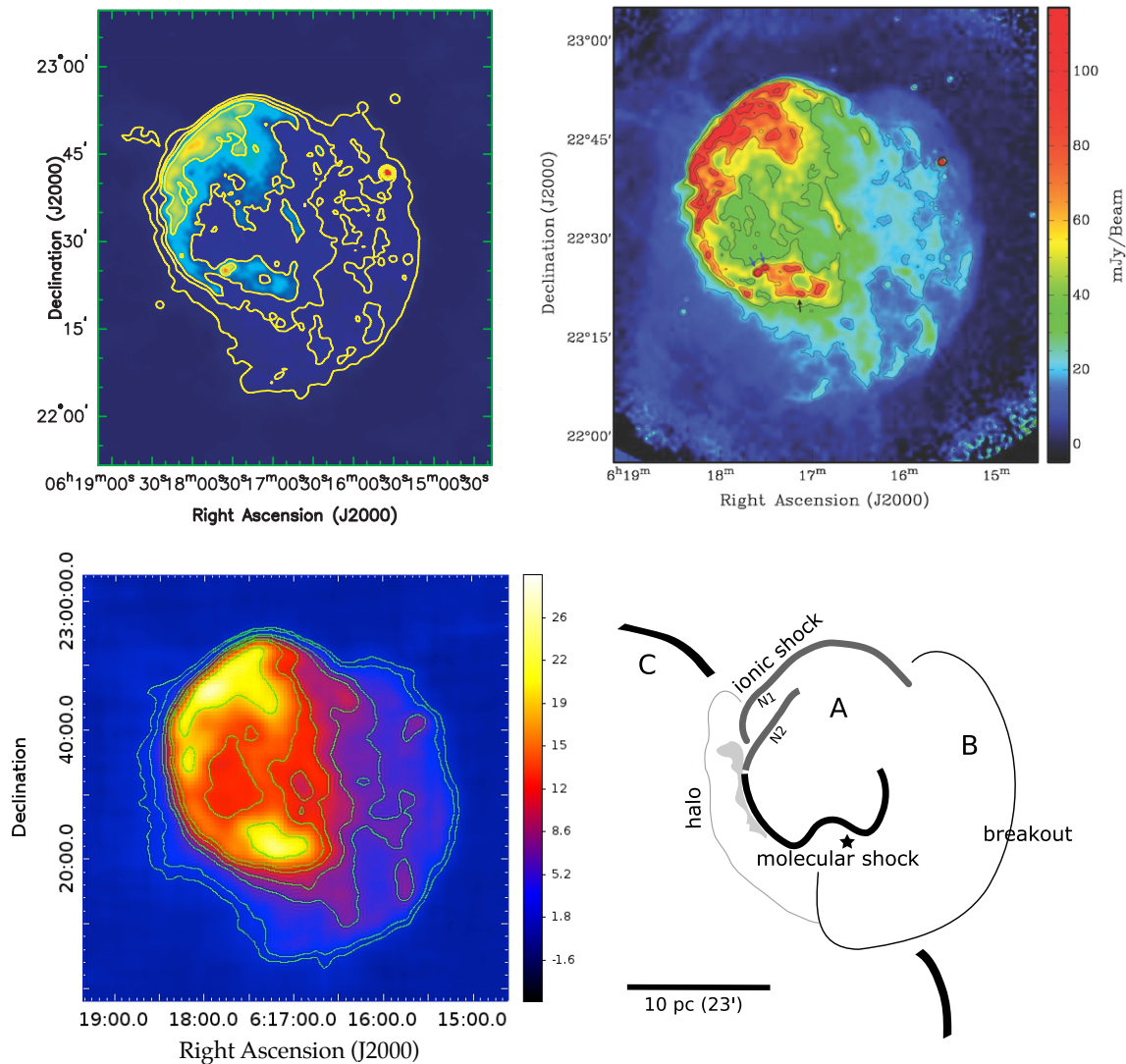
Figure 10: Upper left : 330 MHz continuum map of 3C157 obtained with the VLA (Hewitt et al. 2006). Upper right: 21cm continuum image of 3C157 obtained with the VLA and Arecibo (Lee et al. 2008). The blue arrows indicate the position of the two extragalactic sources and the black one, the pulsar. Bottom left: map of 3C157 obtained at 6.9 GHz with SRT. Bottom right: schematic view of the morphology of 3C157 (Lee et al. 2008). The pulsar is indicated with the asterisk.

The details in the morphology of 3C157 obtained with SRT at 6.9 GHz is comparable with interferometric observations carried out at lower frequencies (330 MHz - 1.4 GHz). 3C157 consists in two nearly concentric shells, referred as shells A and B on Figure 10, presenting a clear difference in the radio continuum intensity. The bulk of the emission comes from the northeastern part of the remnant that forms shell A (in red in Fig.10). This shell is open on the western side on shell B (indicated in light blue), which is much more diffused. This favors the scenario through which shell B is a breakout portion of the supernova remnant into a rarefied medium (Lee et al. 2008).

Shell A presents two very bright emission regions, apparently connected with a ridge. The northern part indicates signatures of atomic/ionic shock (Duin & van der Laan 1975). Some peaks, associated with shocked HI filaments (referred as N1 and N2 in the schematic image in Fig.10) most likely correspond to the projected boundary of the remnant. The bright emission at the southwestern part of the ridge has a different origin.

Various signs of molecular shock of H2 are highlighted (Burton et al. 1988). Two bright extragalactic point-like sources unrelated to the remnant (Braun & Strom 1986) are present near (α,δ)=(06h17m30s, 22°25'). Moreover, the pulsar and its wind nebula, identified by Chandra and the VLA (Olbert et al. 2001) are visible at (α,δ)=(06h17m19s, 22°22'). All of these radio sources constitute the second bright radio emission of shell A.

In contrast with the clearly defined edge on the north of shell A, the southeast boundary of the remnant indicates an extended faint emission beyond shell A, forming a faint halo. Note that the histogram shown in Fig.7 highlights this emission (region *b*), which is different from shell B. This probably originates from the overlap with another remnant, G189.6+3.3 (shell C in Fig.10), but it is still under discussion (Lee et al. 2008). Another notable feature is the filamentary structure in shell B, which corresponds with optical filaments. These filaments are associated with the *c* region in Figure 7.

B) SNR W44

The map resulting from the simultaneous data analysis of the three observations of W44 is presented in Figure 11. As in the case of 3C157, the quality of the map is highly improved by adding the individual maps (RFI subtraction, S/N). A total of 45 passages were performed per beam. However, we still note the presence of some "lines" corresponding to the subscans in declination, at about RA=18:56:30h. These features most likely result from the difficulty to subtract the baseline in the regions close to the Galactic plane, where the SNR is also visible. To be correctly subtracted, the baseline should represent about 40-60% of the subscan, but in these areas, less than 30% is really free of sources. The rms associated with the map is 0.25 counts and the corresponding dynamic range is estimated at 250.8. These values can be compared to those of the individual maps of W44 reported in Table 3.
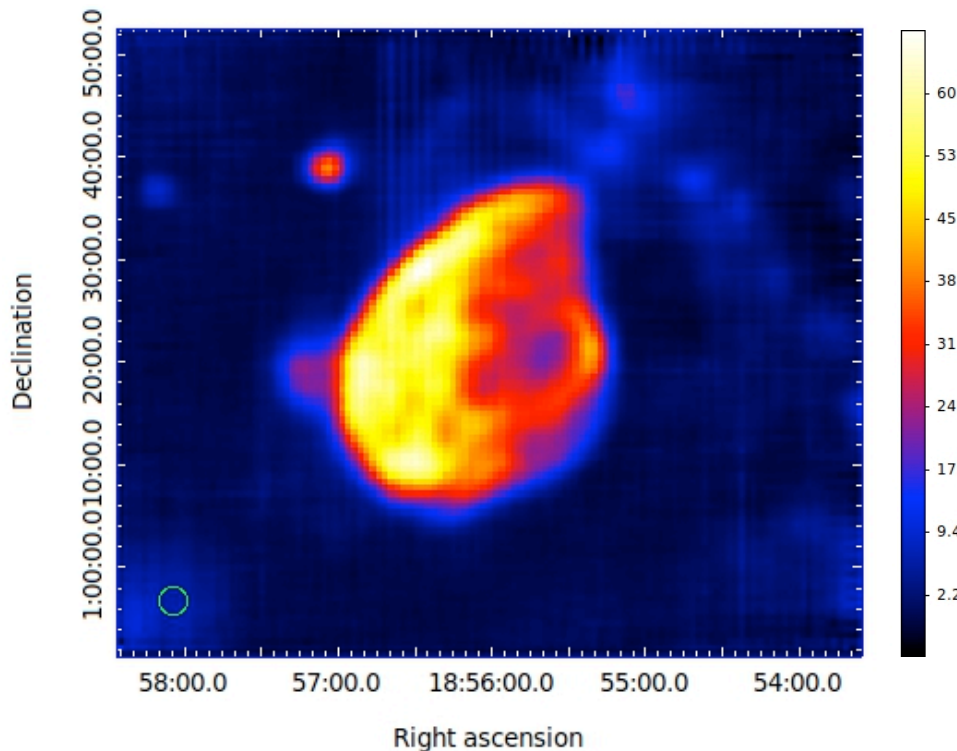

Figure 11: Global map of W44 using the advanced baseline subtraction method on the 3 data sets summarized in Table 2. The 1.2°*1.0° map is composed of 501 RA +608 DEC subscans.

We produce the count histogram corresponding to W44 to better understand the regions where the flux is uniform (see Figure 12). The prominent peak indicates the average rms at about 0.17 counts as for 3C157 (Figure 13), whereas a secondary thin peak is visible at 3 counts (region *b* on Fig.12). Two other minor peaks are present at 13-15 counts (region *c*) and 23-25 counts (region *d*). We plot the contours corresponding to these values on the map of W44. The region delimitated by the contour at 3 counts indicates sources in the Galactic plane.
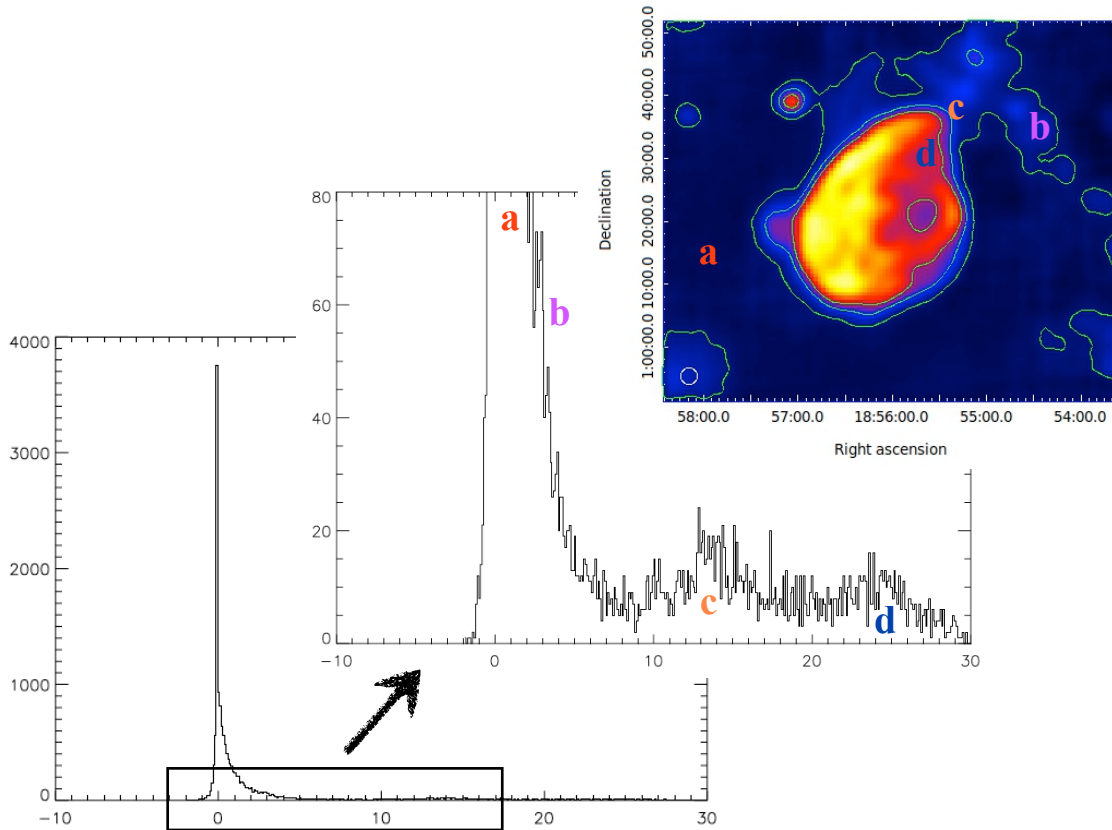

Figure 12: Count histogram obtained with a binning of 0.1. The different peaks (a,b,c,d) indicate regions on the map were the flux is uniform. The corresponding contours are identified on the map of W44.
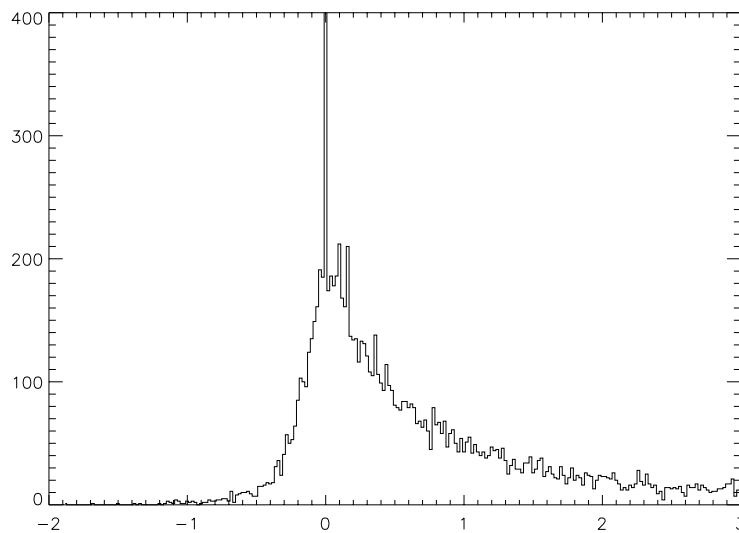
Figure 13: Zoom of the main peak of the count histogram corresponding to W44, with a binning of 0.02. The full width at half maximum of the peak gives an estimate of the average rms (the narrow peak at 0 counts is unphysical and related to the edge of the rectangular map not fully covered by the observations).

We compared the radio continuum maps of W44 obtained with single-dish telescopes (Effelsberg at 4.9 GHz, Urumqi at 4.8 GHz and SRT at 6.9 GHz) with the VLA observations conducted at 1465 MHz and 324 MHz. The observation details are summarized in Table 5.

	Effelsberg	**Urumqi**	**VLA**	**VLA**	**SRT**
Date obs	1974-1975	2004-2009	07/08/1984 09/1985	15/06/2002 14/12/2002 16/03/2003 31/08/2003 01/09/2003	09/07/2014 11/09/2014 16/09/2014
Total Duration			8 h	26.1 h	9.5 h
Frequency	4.9 GHz	4.8 GHz	1465 MHz	324 MHz	6.9 GHz
Bandwidth	500 MHz	600 MHz	12.5 MHz	3.1 MHz	730 MHz
HPBW	2.6'	9.5'		13"	2.7'
Type of obs	Survey of the Galactic plane	Raster map	Configurations C and D	Configurations A, B, C, D 32 channels	OTF - TP

Table 5: Summary of the observations of W44 conducted by Effelsberg, Urumqi, the VLA, and SRT.

A survey of the Galactic plane was made by the Effelsberg telescope at 4.875 GHz (Altenhoff et al. 1978). Scans were taken in galactic latitude over $b=+/-2°$, at a rate of 80'/min, spaced every 1' in galactic longitude. The half-power beamwidth was 2.6', which gives us a direct comparison with SRT at 6.9 GHz (see Figure 14). The maps obtained with both radiotelescopes are very similar. SNR W44 presents strong intensity regions located mainly in the south of the remnant. It is also interesting to note the emission from the Galactic plane.

Another observation of W44 was performed during a polarization survey carried out with Urumqi at 4.8 GHz. Details of the supernova remnant, the Galactic plane, and sources nearby W44 are clearly visible with SRT, whereas W44 appears more extended in the case of Urumqi since the sources in the vicinity of W44 are seen as part of the remnant (see Fig.14). This is related to the beam width associated to Urumqi at 4.8 GHz, which is about 3.5 times larger than that of SRT at 6.9 GHz (9.5' for Urumqi against 2.7' for SRT).

SNR W44

a) Urumqi at 4.8 GHz
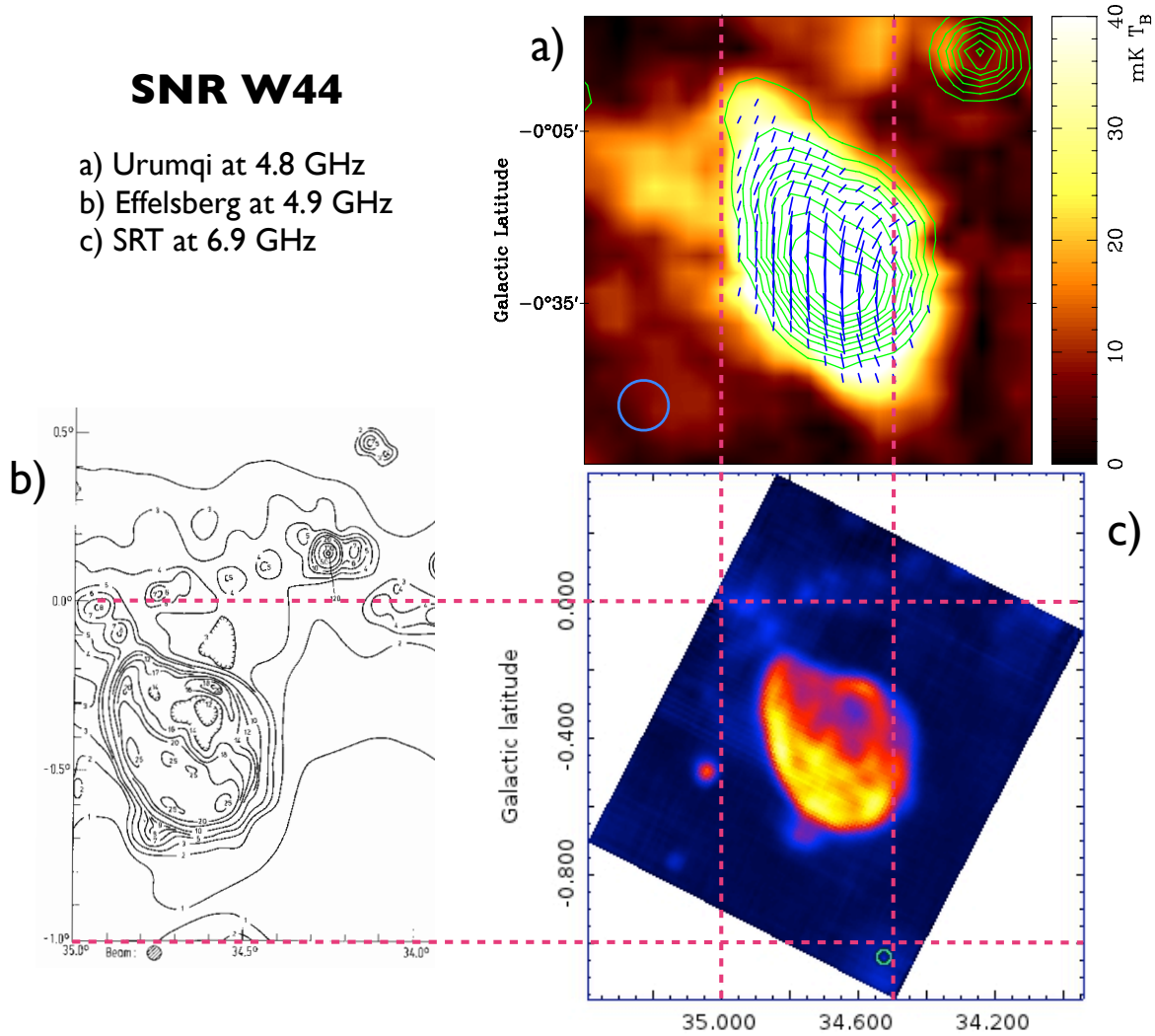b) Effelsberg at 4.9 GHz
c) SRT at 6.9 GHz

Figure 14: Comparison of the radio continuum emission of SNR W44 with single-dish telescopes. a) Intensity contours (indicated in green) obtained with the Urumqi 6cm polarization survey (Sun et al. 2011). b) Contour map obtained by Effelsberg during a survey of the Galactic plane (Altenhoff et al. 1978). c) SRT observation at 6.9 GHz. Dot lines indicate the correspondence between the Galactic coordinates. The blue and green circles in the bottom corner of the maps show the beam size (see Table 5).

In order to examine more in detail the contribution of the sources located in the Galactic plane, we display the brightness profile (see Figure 15) corresponding to the rectangular box plotted on the image of W44 obtained with SRT. The brightest sources produce an emission of about 11 counts, which is not negligible with respect to the emission from the supernova remnant. For comparison, the maximum of the W44 emission is about 66 counts.
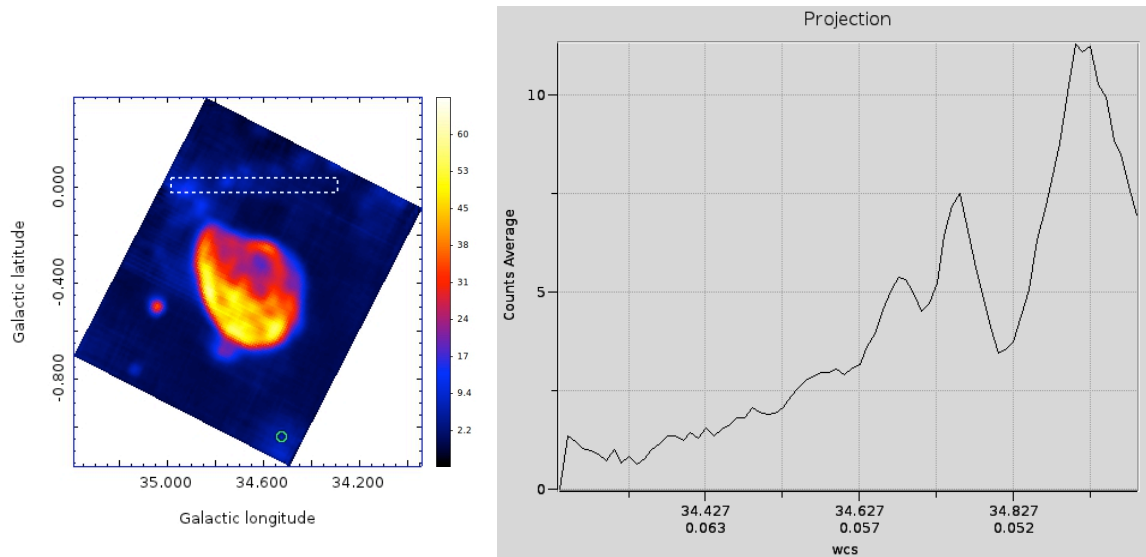
Figure 15: Brightness profile of the Galactic plane corresponding to the rectangular box on the image of W44. Note that the Galactic longitude increases in the opposite directions.

In Figure 16, we compare the map of W44 produced by SRT with high-resolution VLA images of the remnant at 1465 MHz and 324 MHz, using multiple-configurations of the VLA. The VLA images reveal incredible details in the radio morphology of W44, in particular the extreme filamentary and clumpy emission. The brightest filaments are also highlighted with SRT.
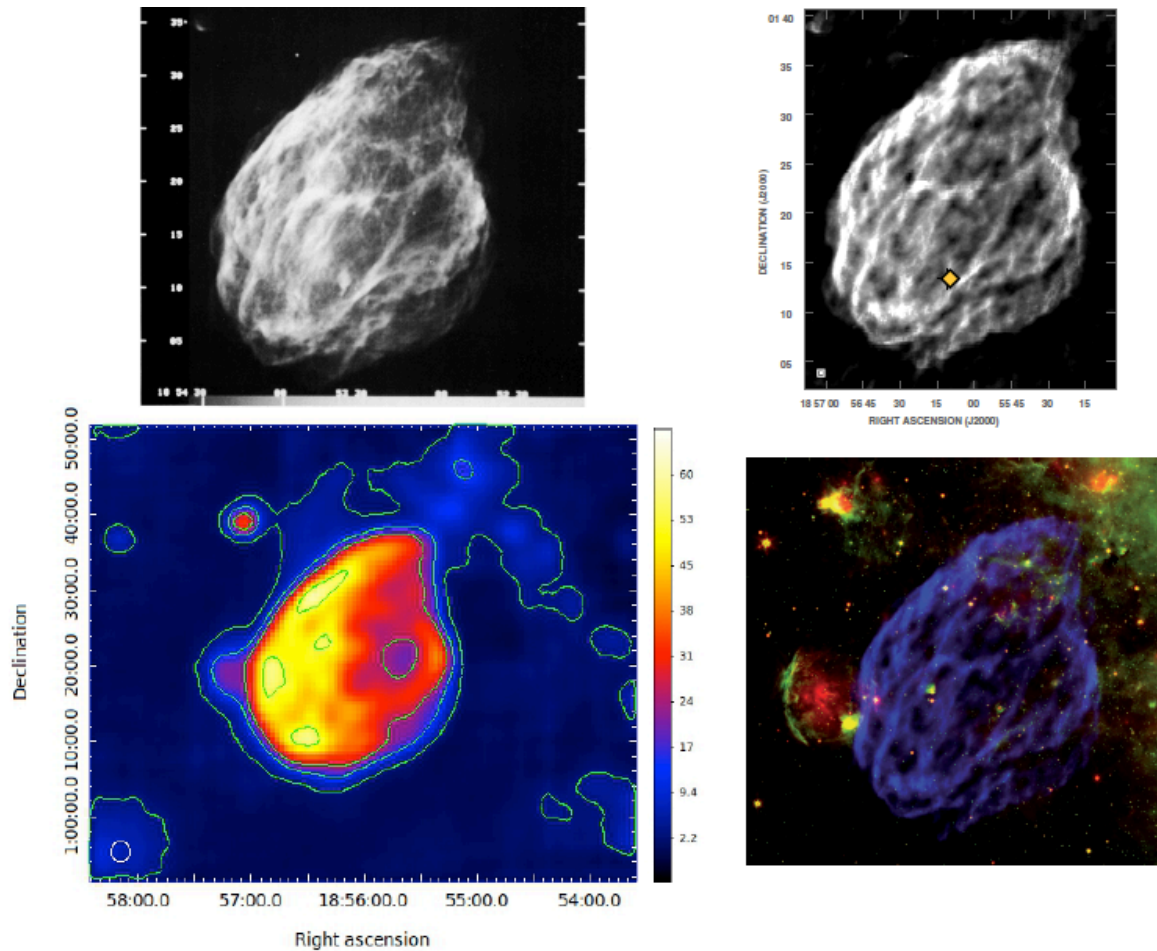
Figure 16: Comparison of the map obtained with SRT (bottom left) with high-resolution images of the radio continuum at 1465 MHz (upper left) and 324 MHz (right images) with the VLA. The yellow point on the upper right map indicates the position of the pulsar PSR B1853+01. Bottom right image: 324 MHz image of the remnant with 13" resolution is shown in blue while the green and red images correspond to the Spitzer 8 and 24 μm data (Castelletti et al. 2007).

The radio emission of W44 is characterized by an asymmetric limb-brightened shell structured in filaments preferentially aligned in the south-est north-west direction. These filaments most likely result from radiative shocks driven into clouds or sheets of dense gas (Jones et al. 1993). The brightest emission occurs along the eastern boundary at about 18h56m50s, 01°17). It results from the interaction between W44 and dense molecular clouds observed in this region (Seta et al. 2004; Reach et al. 2005). Spitzer observations at 24 μm and 8 μm identify a circular HII region centered at 18h56m47.9s, 01°17 54 (named G034.7-00.6; Paladini et al. 2003) with the IRAS point source 18544+0112, which is a young stellar object located on its border.

To the west, a short bright arc is visible at 18h55m20s, 01°22 (Castelletti et al. 2007). It corresponds to the SNR shock colliding with a molecular cloud located in this region, consistent with bright optical filaments and IR observations.

The radio and X-ray nebula associated with the pulsar (Frail et al. 1996; Petre et al. 2002) has a slight offset w.r.t. the pulsar and is consistent with a motion of the pulsar away from the SNR center.

To better understand the morphology of W44, Seta et al. (2004) proposed a schematic illustration of the remnant (top view) to represent the complex interaction of W44 with the surrounding molecular clouds (see Figure 17). Molecular clouds were extensively mapped in CO emission. Several features such as high-velocity line-wing emission, sharp-edged clouds at the CO/SNR interface, broad line emission (SEMBE), and CO emission, are morphologically associated with the radio continuum and/or X-ray emission (Seta et al. 2004).
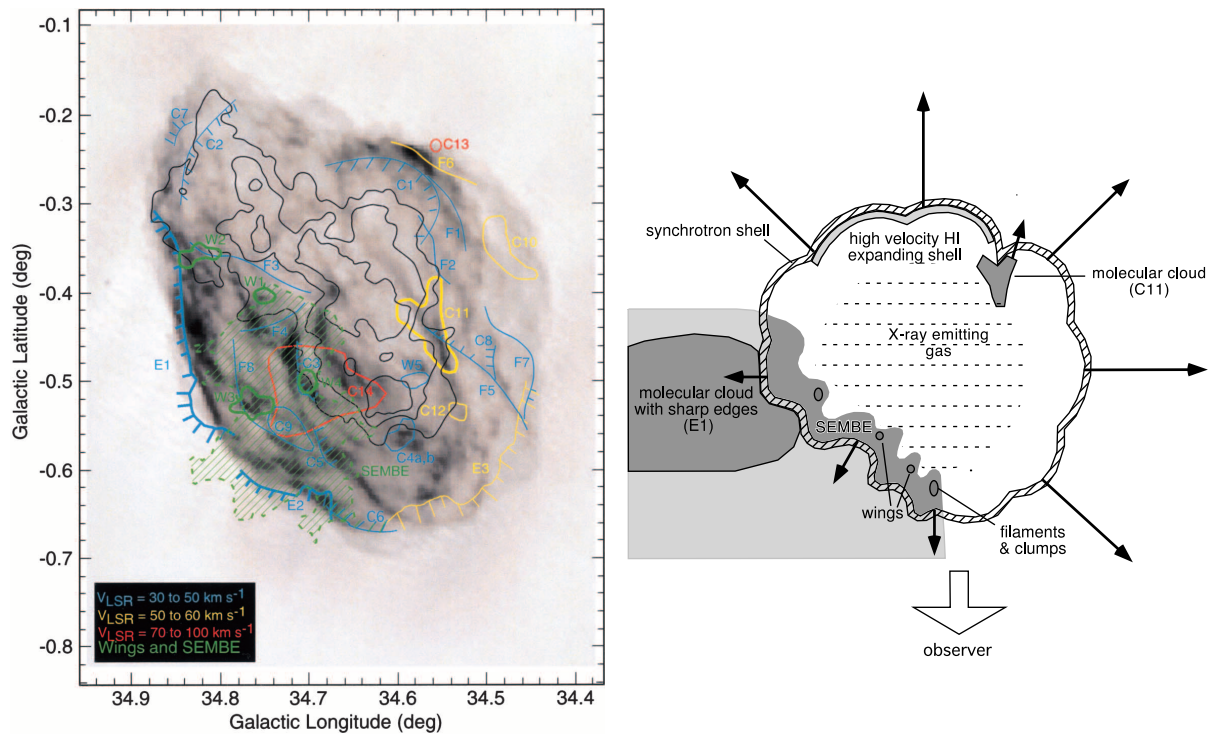

Figure 17: Left: superimposition of the radio continuum emission at 1.4 GHz (grey scale; Jones et al. 1993) with the X-ray emission (black contours; Rho et al. 1994) and the CO features at different velocity ranges (colored contours and lines with labels; Seta et al. 2004). Right: schematic illustration (top view) of W44 based on the CO observations (Seta et al. 2004).

Conclusion

We presented the first maps of the SNR 3C157 and W44 obtained with SRT at 6.9 GHz. The data analysis was performed using the Single Dish Imager (SDI) software, a new tool that demonstrates the capabilities of SRT in performing single-dish images in C-band. SDI offers several degrees of automated data reduction, from the quicklook to the refined methods of the baseline subtraction. It also proposes a powerful method of RFI rejection. The resulting maps provide a detailed structure of the remnants, comparable to interferometric observations carried out with the VLA at lower frequencies. This testifies the excellent performances of SRT in performing maps of extended sources using OTF observations. This is of great interest to infer the flux in different resolved regions of sources. A second AV note will be devoted to the flux calibration of the SNR 3C157 and W44 maps presented here.

Open issues

- Providing different maps separately for the two IF;
- Final assessment of gain stability in C-band imaging;
- Correlation among weather condition/opacity and baseline slope;
- Defining weather standards/opacity for C-band OTF SRT imaging;
- Final schedule optimization (map repetition with off-sets among subscans);

References

Altenhoff W.J., Downes D., Pauls T. and Schraml J. 1979, A&AS, 35, 23

Burton M.G., Geballe T.R., Brand P.W.J.L. and Webster A.S. 1988, MNRAS, 231, 617

Braun R. & Strom R.G. 1986, A&A, 164, 193

Castelletti G., Dubner G., Brogan C. and Kassim N.E. 2007, A&A, 471, 537

Duin R.M. & van der Laan H. 1975, A&A, 40, 111

Frail D.A., Giacani E.B., Goss W.M. & Dubner G. 1996, ApJ, 464, 165

Gao X.Y., Han J.L., Reich W. et al. 2011, A&A, 5291, A159

Green D.A. 2014, *"A Catalogue of Galactic Supernova Remnants (2014 May version)"* (http://www.mrao.cam.ac.uk/surveys/snrs/)

Heiles C. 1984, ApJS, 55, 585

Hewitt J.W., Yusef-Zadeh F., Wardle M. et al. 2006, ApJ, 652, 1288

Jones L. R., Smith A. & Angellini L. 1993, MNRAS, 265, 631

Lee J.J., Koo B.C., Yun M.S. et al. 2008, AJ, 135, 796

Olbert C.M., Clearfield C.R., Williams N.E. et al. 2001, ApJ, 554, 205

Paladini R., Burigana C., Davies R.D. et al. 2003, A&A, 397, 213

Petre R., Kuntz, K.D., Shelton R.L. 2002, ApJ, 579, 404

Reach W.T., Rho J. and Jarrett T.H. 2005, ApJ, 618, 297

Reich W., Zhang X. and Furst E. 2003, A&A, 408, 961

Righini S., Orlati A. and Poppi S. 2015, *"Observing at the SRT with Nuraghe"*

Rho J., Petre R., Schlegel E.M. & Hester J. J. 1994, ApJ, 430, 757

Seta M., Hasegawa T., Sakamoto S. et al. 2004, AJ, 127, 1098

Seta M., Hasegawa T., Dame T.M. et al. 1998, ApJ, 505, 286

Smith A., Jones L.R., Watson M.G. et al. 1985, MNRAS, 217, 99

Snell R.L., Hollenbach D., Howe J.E. et al. 2005, ApJ, 620, 758

Sun X. H., Reich P., Reich W. et al. 2011, A&A, 536, A83

Vacca V., Iacolina M.N., Pellizzoni A. et al. 2013, Internal Report INAF-IRA 468/13

Wolszczan A., Cordes J.M. and Dewey R.J. 1991, ApJ, 372, 99

Appendix

- links to AV test repositories: schedules, ds9 fits images, jpeg images, data (to be done)

Images acknowledgement policy

The above material (including figures) can be presented at congresses or papers by SRT team/board members mentioning the following acknowledgement:

"Results obtained through the SRT Dingle-Dish Imager (SDI) in the frame of AV test C-band observations of supernova remnants with SRT (Internal Report AV-REP-006; Egron, Pellizzoni, Iacolina et al. 2015)".